

Gravitational radiation from the coalescence of binary neutron stars: Effects due to the equation of state, spin, and mass ratio

Xing Zhuge, Joan M. Centrella, and Stephen L. W. McMillan

Department of Physics and Atmospheric Science, Drexel University, Philadelphia, Pennsylvania 19104

(Received 17 June 1996)

We calculate the gravitational radiation produced by the coalescence of inspiraling binary neutron stars in the Newtonian regime using three-dimensional numerical simulations. The stars are modeled as polytropes and start out in the point-mass regime at wide separation. The hydrodynamic integration is performed using smooth particle hydrodynamics with Newtonian gravity, and the gravitational radiation is calculated using the quadrupole approximation. We have run a number of simulations varying the neutron star radii, equations of state, spins, and mass ratio. The resulting gravitational waveforms and spectra are rich in information about the hydrodynamics of coalescence, and show characteristic dependence on GM/Rc^2 , the equation of state, and the mass ratio. [S0556-2821(96)05424-0]

PACS number(s): 04.30.Db, 04.80.Nn, 95.85.Sz, 97.80.Gm

I. INTRODUCTION

Coalescing binary neutron stars are among the most promising sources of gravitational waves for detection by interferometers such as the Laser Interferometric Gravitational-wave Observatory (LIGO) [1], VIRGO [2], and GEO [3]. Recent studies [4] suggest that binary inspiral due to gravitational radiation reaction, and the eventual coalescence of the component stars, may be detectable by these instruments at a rate of several per year. The inspiral phase comprises the last several thousand binary orbits and covers the frequency range $f \sim 10\text{--}1000$ Hz, where the broadband interferometers are most sensitive. During this stage, the separation of the stars is much larger than their radii and the gravitational radiation can be calculated using post-Newtonian expansions in the point-mass limit [5]. Analysis of the inspiral waveform is expected to reveal the masses and spins of the neutron stars, as well as the orbital parameters of the binary systems [6–9].

When the binary separation is comparable to the neutron star radius, hydrodynamic effects become dominant and coalescence takes place within a few orbits. The coalescence regime probably lies at or beyond the upper end of the frequency range accessible to broadband detectors, but it may be observed using specially designed narrow band interferometers [10] or resonant detectors [11]. Such observations may yield valuable information about neutron star radii, and thereby the nuclear equation of state [8,12,13].

Three-dimensional numerical simulations are needed to study the detailed hydrodynamical evolution of the coalescence. Shibata, Nakamura, and Oohara [14,15] have studied the behavior of binaries with both synchronously rotating and nonrotating stars, using an Eulerian code with gravitational radiation reaction included. Ruffert *et al.* [16] have also used Eulerian methods with radiation reaction included to study coalescence of neutron stars with a physical equation of state and various spins. Rasio and Shapiro [17,18] have simulated the coalescence of synchronously rotating neutron-star binaries using the Lagrangian smooth particle hydrodynamics (SPH) method with purely Newtonian grav-

ity. Davies *et al.* [19] have carried out SPH simulations of the inspiral and coalescence of nonsynchronously rotating neutron stars, focusing on the thermodynamics and nuclear physics of the coalescence. All of these studies used the quadrupole approximation to calculate the gravitational radiation emitted. Finally, Wilson, Mathews, and Marronetti [20] have developed an Eulerian code that incorporates general relativistic effects in the limit in which the metric remains conformally flat and gravitational radiation is neglected. A multipole expansion is used to calculate the gravitational radiation.

We have carried out three-dimensional (3D) simulations of binary neutron star coalescence in the Newtonian regime using SPH, with particular application to the resulting gravitational wave energy spectrum dE/df . The neutron stars are initially modeled as spherical polytropes on circular orbits, with separations sufficiently large that tidal effects are negligible. The stars thus start out effectively in the point-mass regime. The gravitational field is purely Newtonian, with the gravitational radiation calculated using the quadrupole approximation. To cause the stars to spiral in, we mimic the effects of gravitational radiation reaction by introducing a frictional term into the equations of motion to remove orbital energy and angular momentum at the rate given by the equivalent point-mass inspiral. As the neutron stars get closer together the tidal distortions grow and eventually dominate, and coalescence quickly follows. The resulting gravitational wave forms match smoothly onto the point-mass inspiral wave forms, facilitating analysis in the frequency domain. In paper I [21] we considered equal mass neutron stars with $M = 1.4M_{\odot}$ and varied the neutron star radius and equation of state. We demonstrated that the resulting gravitational wave signatures are rich in information about the hydrodynamics of coalescence and are sensitive to both GM/Rc^2 and the equation of state. In this paper, we extend our study to include the effects of unequal masses as well as spin.

It is important to understand the context of these models. Our work is carried out in the Newtonian regime and therefore is a first step toward understanding the gravitational ra-

diation signatures of binary coalescence. With these simplified models we are able to study binaries that start out with fairly wide separations and make ~ 3 orbits before contact, and to concentrate on the hydrodynamical properties of the merger. Of course, the Newtonian approximation does break down for systems involving neutron stars, since $GM/Rc^2 \sim 0.2$ for a typical neutron star of mass $M = 1.4M_\odot$ and radius $R = 10$ km. General relativistic effects can therefore be expected to play an important role in the final stages of inspiral and coalescence [22], and Newtonian results must be viewed with appropriate caution. We believe that Newtonian models provide an interesting first look at the properties of coalescence waveforms and spectra. In addition, they can be used for comparison with general relativistic calculations to help determine where relativistic effects become important and how they show up in the resulting gravitational waveforms and spectra. Finally, the valuable experience gained in carrying out these Newtonian calculations is important for the development of fully general relativistic models.

This paper is organized as follows. In Sec. II we present a brief description of the techniques used in our simulations. The use of frictional terms in the equations of motion to mimic the effects of gravitational radiation reaction is discussed in Sec. III. Section IV revisits the standard model (with identical neutron stars having masses $M = 1.4M_\odot$ and radii $R = 10$ km), extending and expanding the analysis begun in paper I. The effects of changing the neutron star radius, equation of state, and spin are examined in Sec. V. Binaries with unequal mass components are considered in Sec. VI. Finally, Sec. VII contains a summary and discussion of our results.

II. SIMULATION TECHNIQUES

The methods we used to produce our models have been presented in some detail in paper I [21] and Ref. [23]. We therefore give a only brief description of these methods in this section, and refer the reader to the literature for further information.

Lagrangian techniques such as SPH [24] are especially attractive for modeling neutron star coalescence since the computational resources can be concentrated where the mass is located instead of being spread over a grid that is mostly empty. We have used the implementation of SPH by Hernquist and Katz [25] known as TREESPH. In this code, the gravitational field is purely Newtonian, and a hierarchical tree method [26] optimized for vector computers is used to calculate the gravitational forces. This leads to a significant gain in efficiency and allows the use of larger numbers of particles than would be possible with methods that simply sum over all possible pairs of particles.

We calculate the gravitational radiation quantities in the quadrupole approximation, which is valid for nearly Newtonian sources [27]. The reduced (i.e., traceless) quadrupole moment of the source is given by

$$I_{ij} = \int \rho \left(x_i x_j - \frac{1}{3} \delta_{ij} r^2 \right) d^3 r, \quad (1)$$

where $i, j = 1, 2, 3$ are spatial indices and $r = (x^2 + y^2 + z^2)^{1/2}$ is the distance to the source. For an observer situated on the

axis at $\theta = 0, \phi = 0$ of a spherical coordinate system with its origin located at the center of mass of the source, the gravitational wave amplitudes for the two polarization states are given by

$$h_+ = \frac{G}{c^4} \frac{1}{r} (\ddot{I}_{xx} - \ddot{I}_{yy}), \quad (2)$$

$$h_\times = \frac{G}{c^4} \frac{2}{r} \ddot{I}_{xy}. \quad (3)$$

Here, an overdot indicates a time derivative d/dt . The standard definition of gravitational-wave luminosity is

$$L = \frac{dE}{dt} = \frac{1}{5} \frac{G}{c^5} \langle \langle \dot{I}_{ij}^{(3)} \dot{I}_{ij}^{(3)} \rangle \rangle, \quad (4)$$

where there is an implied sum on i and j , the superscript (3) indicates the third time derivative, and the double angle brackets indicate an average over several wave periods. Since such averaging is not well defined during coalescence, we simply display the unaveraged quantity $(G/5c^5) \dot{I}_{ij}^{(3)} \dot{I}_{ij}^{(3)}$ in the plots below. The gravitational wave energy spectrum dE/df , which gives the energy emitted as gravitational radiation per unit frequency interval, is a key diagnostic tool for understanding the results of our simulations. It is given by Thorne [28] in the form

$$\frac{dE}{df} = \frac{c^3}{G} \frac{\pi}{2} (4\pi r^2) f^2 \langle |\tilde{h}_+(f)|^2 + |\tilde{h}_\times(f)|^2 \rangle, \quad (5)$$

where $\tilde{h}(f)$ is the Fourier transform of $h(t)$, and the angle brackets denote an average over all source angles. See paper I for details.

We use the techniques of [23] to calculate the reduced quadrupole moment I_{ij} and its derivatives. In particular, \dot{I}_{ij} and \ddot{I}_{ij} are obtained using particle positions, velocities, and accelerations already present in the code to produce very smooth waveforms. This yields expressions similar to those of Finn and Evans [29]. However, $\dot{I}_{ij}^{(3)}$ requires the derivative of the particle accelerations, which must be determined numerically and introduces noise into the gravitational-wave luminosity L . We have applied smoothing to reduce this noise in producing all graphs of L in this paper; see [23] for further discussion.

The neutron stars are initially modeled as widely separated polytropes with equation of state

$$P = K \rho^\Gamma = K \rho^{1+1/n}, \quad (6)$$

where K is a constant that measures the specific entropy of the material and n is the polytropic index. The stars are placed on orbits with wide enough separation that tidal effects are negligible. An individual star may be allowed to be in uniform rotation about an axis through its center of mass. We take the direction of this spin angular velocity Ω_s (which is measured in an inertial frame) to be either parallel or antiparallel to the direction of the orbital angular momentum. Because the time scale for tidal effects to develop is far greater than the dynamical time t_D for an individual star, where

$$t_D = \left(\frac{R^3}{GM} \right)^{1/2}, \quad (7)$$

we start with stable, ‘‘cold’’ polytropes. The nonrotating stars ($\Omega_s=0$) were produced by the method discussed in [23]. The rotating stars were produced using the method described in [30] and [31].

III. MODELING INSPIRAL BY GRAVITATIONAL RADIATION REACTION

Widely separated binary neutron stars (that is, with separation $a \gg R$) spiral together due to the effects of energy loss by gravitational radiation reaction. Once the two stars are close enough for tidal distortions to be significant, hydrodynamical effects dominate and rapid inspiral and coalescence ensue. In our calculations the neutron stars are placed on (nearly) circular orbits with wide enough separation that the stars are effectively in the point-mass limit. Since the gravitational field is purely Newtonian and does not take radiation reaction into account, we must explicitly include these losses to cause inspiral until hydrodynamical effects take over.

We accomplish this by adding a frictional term to the particle acceleration equations to remove orbital energy at a rate given by the point-mass inspiral expression (see [19] for a similar approach). The gravitational wave luminosity for point-mass inspiral on circular orbits is [27,32]

$$L_{\text{PM}} = \frac{dE}{dt} \Big|_{\text{PM}} = \frac{32}{5} \frac{G^4}{c^5} \frac{\mu^2 \mathcal{M}^3}{a^5}, \quad (8)$$

where $\mathcal{M} = M_1 + M_2$ is the total mass of the system, $\mu = M_1 M_2 / \mathcal{M}$ is the reduced mass, and the subscript ‘‘PM’’ refers to point-mass inspiral. We assume that this energy change is due to a frictional force \vec{f} that is applied at the center of mass of each star, so that each point in the star feels the same frictional deceleration. For star 1, we obtain

$$\vec{f}_1 \cdot \vec{V}_1 = \left(1 + \frac{M_1}{M_2} \right)^{-1} \frac{dE}{dt} \Big|_{\text{PM}}, \quad (9)$$

where \vec{V}_1 is the center-of-mass velocity of star 1; an analogous expression in which the subscripts ‘‘1’’ and ‘‘2’’ are interchanged holds for star 2. Since \vec{f}_1 acts in the direction opposite to \vec{V}_1 this gives an acceleration

$$\vec{a}_1 = \frac{\vec{f}_1}{M_1} = - \frac{1}{\mathcal{M}} \frac{M_2}{M_1} \frac{dE}{dt} \Big|_{\text{PM}} \frac{\vec{V}_1}{|\vec{V}_1|^2} \quad (10)$$

for star 1 and similarly for star 2. These frictional terms are added to the particle acceleration so that all particles in a given star experience the same frictional deceleration. The net effect is that the centers of mass of the stars follow trajectories that approximate point-mass inspiral. The frictional terms are applied until tidal effects dominate, leading to more rapid inspiral and coalescence by purely Newtonian hydrodynamical processes [33]. For each of the runs reported in this paper, we determine the optimal time to turn off the frictional terms experimentally; see paper I for details. (Operationally, our assignment of a particle to a ‘‘star’’ is based

simply on which body it happened to belong to initially. Since the frictional term is turned off before coalescence occurs, the question of what to do after the stars have merged does not arise.)

The stars are initially placed on the x axis on a counter-clockwise circular orbit with separation a_0 in the center-of-mass frame of the system in the $x-y$ plane. Thus, the center of mass of M_1 is located at (x, y) position $(a_1, 0)$ and that of M_2 is located at $(-a_2, 0)$, where $a_0 = a_1 + a_2$, $a_1 = a_0 \mu / M_1$ and similarly for a_2 [32]. The stars are then given the equivalent point-mass circular velocities $V_{y,1} = (G/\mathcal{M}a_0)^{1/2} M_2$ and $V_{y,2} = -(G/\mathcal{M}a_0)^{1/2} M_1$.

To ensure that the stars start out on the correct point-mass inspiral trajectories, we also give them an initial inward radial velocity V_x as follows. For point-mass inspiral the separation $a(t)$ is given by [27]

$$a(t) = a_0 \left(1 - \frac{t}{\tau_0} \right)^{1/4}, \quad (11)$$

where a_0 is the separation at the initial time $t=0$ and

$$\tau_0 = \frac{5}{256} \frac{c^5}{G^3} \frac{a_0^4}{\mu \mathcal{M}^2} \quad (12)$$

is the inspiral time, i.e., the time needed to reach separation $a=0$. We write

$$V_r = \frac{da}{dt} \Big|_{t=0} = \frac{64}{5} \frac{G^3}{c^5} \frac{\mu \mathcal{M}^2}{a_0^3}. \quad (13)$$

Requiring the center of mass of the binary system to have zero velocity then gives $V_{x,1} = -(M_2/\mathcal{M})V_r$ and $V_{x,2} = (M_1/\mathcal{M})V_r$. The use of the correct initial inspiral trajectory allows us to match our gravitational waveforms smoothly to the equivalent point-mass waveforms. This is important when analyzing the signals in the frequency domain.

IV. BINARY COALESCENCE: THE STANDARD MODEL

We begin by examining binary coalescence for the case of equal mass neutron stars with masses $M_1 = M_2 \equiv M = 1.4M_\odot$, radii $R_1 = R_2 \equiv R = 10$ km (so $GM/Rc^2 = 0.21$), and polytropic index $n=1$ ($\Gamma=2$). The stars start out with zero spin ($\Omega_s=0$) on (nearly) circular orbits with initial separation $a_0 = 40$ km in the point-mass limit. Time is measured in units of the dynamical time t_D for a single star using Eq. (7); here, $t_D = 7.3 \times 10^{-5}$ s. We consider this to be our standard run and refer to it as Run 1; the parameters of this model are summarized in Table I. This run was first discussed in paper I, which also included tests of our numerical method with varying particle number and artificial viscosity coefficients. In this section we revisit the standard model, extending and expanding the analysis begun in paper I, defining our terminology, and reintroducing some key features of the problem.

A. General features of the coalescence

The evolution of this model with $N=4096$ particles per star is shown in Fig. 1. In each frame all particles are pro-

TABLE I. Parameters of the models are given. For all runs, $M_1=1.4M_\odot$. The mass ratio is $q=M_2/M_1$, the stellar radii are R_1 and R_2 , and the initial separation is a_0 . The dynamical time t_D is calculated using the parameters of star 1. T_s gives the spin period of each star, with a positive (or negative) value denoting a spin in the same (or opposite) direction as the orbital angular momentum. The polytropic index n and the Γ refer to the equation of state. Each star contains N SPH particles.

Model	q	R_1 (km)	R_2 (km)	a_0 (km)	t_D (ms)	$T_{s,1}$ (ms)	$T_{s,2}$ (ms)	n	Γ	N
Run 1	1	10	10	40	0.073	0	0	1	2	4096
Run 2	1	15	15	60	0.13	0	0	1	2	1024
Run 3	1	10	10	45	0.073	0	0	1/2	3	4096
Run 4	1	10	10	40	0.073	0	0	3/2	5/3	2048
Run 5	1	10	10	40	0.073	2.6	2.6	1	2	4055
Run 6	1	10	10	40	0.073	2.6	-2.6	1	2	4055
Run 7	0.85	10	10	40	0.073	0	0	1	2	4096
Run 8	0.85	10	9.7	40	0.073	0	0	1/2	3	4096
Run 9	0.5	10	10	40	0.073	0	0	1	2	4096
Run 10	0.5	10	8.7	40	0.073	0	0	1/2	3	4096

jected onto the $x-y$ plane. As the stars spiral together, their tidal bulges grow. By $t=100t_D$, the center-of-mass separation of the two stars is $\sim 2.5R$. At this point the stars undergo a dynamical instability driven by Newtonian tidal forces [33], causing the stars to fall together faster than they would on point-mass orbits. We therefore turn off the frictional term in the code at $t=100t_D$ and follow the rest of the evolution using purely Newtonian hydrodynamics and gravity. The stars rapidly merge and coalesce into a rotating barlike structure. Spiral arms form as mass is shed from the ends of the bar. Angular momentum is transported outward by gravi-

tational torques and lost to the spiral arms. The arms expand and merge to form a disk around the central object. At the end of the run, the system is roughly axisymmetric.

The tidal interactions between the stars increase as they spiral together. Even in the absence of fluid viscosity, Lai and Shapiro [34] have shown that a dynamical tidal lag angle α_{dyn} develops due to the finite time needed for the structure of the stars to adjust to the rapidly changing tidal potential. This leads to the formation of tidal bulges that are not directly aligned, and the resulting gravitational torques cause each star to spin. As the stars spiral together and the separa-

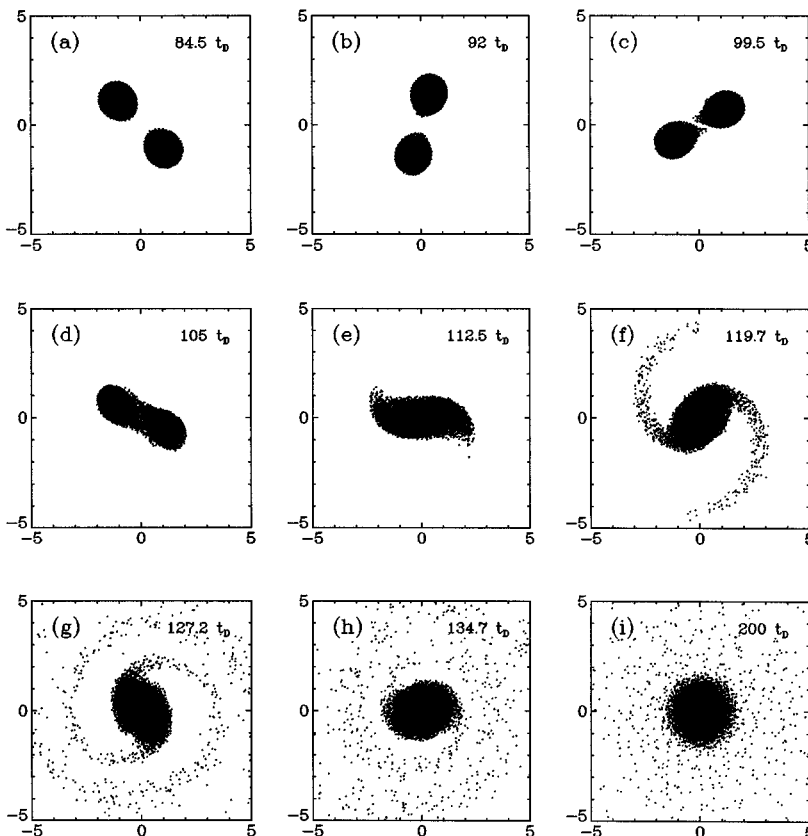


FIG. 1. Particle positions are shown projected onto the $x-y$ plane for Run 1. Here, $M=1.4M_\odot$, $R=10$ km, $\Gamma=2$, and $t_D=0.073$ ms. The initial separation $a_0=4R$. The stars are orbiting in the counterclockwise direction. The vertical axis in each frame is y/R and the horizontal axis is x/R .

tion decreases, α_{dyn} becomes larger. In Fig. 1(c) we estimate the lag angle of the stars near contact to be $\sim 15^\circ$. For non-spinning stars with the parameters of Run 1, Lai and Shapiro [34] find $\alpha_{\text{dyn}} \sim 12^\circ$ at contact, in good agreement with our results.

Now consider the coalescence in a reference frame corotating with the binary. As seen from this corotating frame, the stars appear to be spinning in opposite directions. As the stars begin to merge, the fluid in star 1 is moving in the direction opposite to the fluid in star 2 at the point of contact. This velocity difference over a short spatial scale gives rise to a shear layer between the stars, which is subject to the Kelvin-Helmholtz instability [35,36]. For real neutron stars, vortices can form within this layer on small scales; these eddies can grow and merge together, and turbulence can develop. The behavior of this turbulent region can be important in determining the mixing of the material from the individual neutron stars to produce a final remnant. For example, a turbulent viscosity could be generated and thereby the final configuration may not be irrotational.

However, these processes are difficult to model accurately using 3D numerical simulations due to their limited resolution [37,38]. For example, vortices can form on spatial scales determined by the resolution of the model and spurious numerical shear viscosity, rather than on the smaller physical scales expected in real fluids. These shortcomings must be taken into account when interpreting the results of numerical models of binary coalescence.

We have examined our simulations to see if these effects are occurring. We find that, as the stars merge, a couple of eddies form across the shear layer where the two stars meet. By $t \sim 127t_{\text{D}}$ [Fig. 1(g)], the stars have coalesced to the point that there is only a single density maximum at the center of the remnant. Each star in Run 1 has $N=4096$, giving an effective resolution of $\sim N^{1/3}=16$ particles across the diameter of each star. The Eulerian models of Ruffert, Janka, and Schäfer [16] have somewhat better resolution with the diameter of a single star covering $\sim 20\text{--}40$ zones. Their calculations show the development of two eddies across the shear layer. Recent work by Rasio [38], using SPH with a larger N and increased resolution of the shear layer due to the placement of many smaller mass particles in the outer regions of each star, shows the development of more eddies on smaller scales.

For these reasons, we suspect that numerical effects may be influencing the behavior of the shear layer in our models. For example, they might cause the stars to mix more rapidly than they would in reality. Also, the bar phase of the evolution might be of shorter duration, and the final remnant might have different properties. However, Ruffert *et al.* [16] point out that, in real neutron stars, the Kelvin-Helmholtz mechanism may develop into the macroscopic regime on the spatial scale of the coalescing stars as the eddies grow and merge. This could produce a final flow pattern similar to that seen in the simulations. They also suggest alternative explanations for the development of the final flow pattern. Clearly, more work is needed to resolve these issues. In particular, simulations with many more particles (and more grid zones in the Eulerian case) need to be done.

The two neutron stars merge to form an object of total mass $\sim 2.8M_\odot$, with $\sim 94\%$ ($\sim 2.6M_\odot$) of the matter and

$\sim 74\%$ of the angular momentum in a central core $\varpi \lesssim 2R$, and the remainder in a disk (see paper I). As the evolution proceeds, the core mass and angular momentum remain nearly constant, while the angular momentum in the disk is transported outward due to the effects of gravitational torques. By the end of the simulation at $t=200t_{\text{D}}$, the central core is axisymmetric with material on the edge of the remnant at $\varpi \sim 2R$ rotating at $\Omega \sim 0.6t_{\text{D}}^{-1}$, near the critical angular velocity for breakup. We believe the reason for this axisymmetry can be understood as follows. Consider an equilibrium sequence of uniformly rotating axisymmetric polytropes parametrized by $\beta = T_{\text{rot}}/|W|$, where T_{rot} is the rotational kinetic energy and W is the gravitational potential energy. As β is increased along such a sequence, a point is eventually reached at which mass is lost at the equator. Uniformly rotating polytropes with $n \geq 0.808$ ($\Gamma \leq 2.24$) reach this mass-shedding limit before the point at which ellipsoidal configurations can exist [39,40]. Although the central core in our simulation does show differential rotation, we believe that a similar mechanism is operating here, causing the core to be essentially axisymmetric at the end of the run.

Stable, nonrotating neutron stars are believed to have a maximum mass in the range $\sim 1.4M_\odot$ to $\sim 2.2M_\odot$ [41,42], depending on the equation of state. Rotation can increase this by up to $\sim 17\%$, yielding a maximum mass $\lesssim 2.6M_\odot$ [43,44] (again depending on the equation of state), for rotation near breakup speed. Because the gravitational field in these models is purely Newtonian, the merged remnant in these simulations cannot collapse to a black hole. However, since the final core mass is greater than or comparable to the maximum allowed neutron star mass, general relativity may cause a black hole to form.

The ability of rotation to prevent gravitational collapse to a black hole can be estimated by examining the dimensionless parameter $\mathcal{A} = cJ/G\mathcal{M}^2$, where \mathcal{M} refers to the mass of the entire system. Piran and Stark [45] modeled the gravitational collapse of rigidly rotating polytropes with $\Gamma=2$ and $0 \leq \mathcal{A} \leq 1.5$ using a fully general relativistic 2D axisymmetric code. They found that for $\mathcal{A} < \mathcal{A}_{\text{crit}}$, the collapsing object formed a black hole, whereas for $\mathcal{A} > \mathcal{A}_{\text{crit}}$ the collapse was halted by centrifugal forces leading to a bounce with no black hole formation. For the cases they considered, they found $\mathcal{A}_{\text{crit}} \approx 0.8\text{--}1.2$.

It is interesting to estimate the value of \mathcal{A} for our simulations. Since this rotation parameter is a general relativistic concept and the values of J and \mathcal{M} that we determine from our simulations are purely Newtonian, this discussion must be treated with caution. With these caveats, we can examine Fig. 2, which shows \mathcal{A} versus cylindrical radius ϖ for several times during the coalescence of Run 1. At $t = 127t_{\text{D}}$, the innermost regions have $\mathcal{A} > 1$. As the evolution proceeds, gravitational torques transport angular momentum outward and the central value of \mathcal{A} drops. In all cases, $\mathcal{A} < \mathcal{A}_{\text{crit}}$ at the core radius $\varpi \sim 2R$. Thus, our Newtonian results indicate that it is likely a black hole will form. Of course, a firm determination of the final result of binary neutron star coalescence must await a fully general relativistic calculation.

B. Properties of the emitted gravitational radiation

Figure 3(a) shows the gravitational waveform rh_+ for an observer located on the axis at $\theta = \phi = 0$ at distance r from

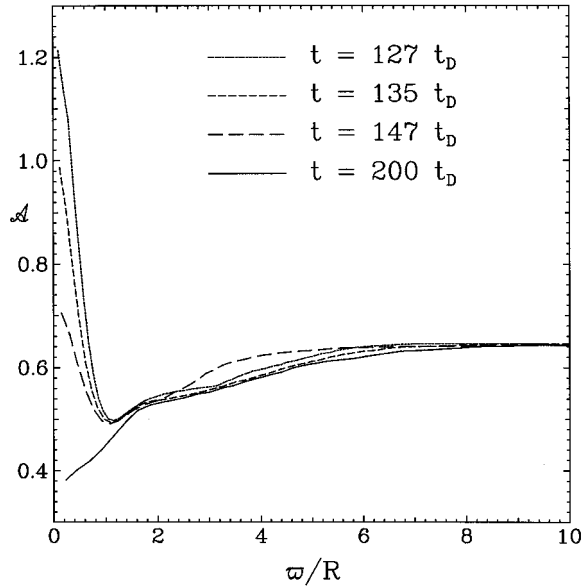


FIG. 2. The dimensionless parameter $\mathcal{A} = cJ/GM^2$, where \mathcal{M} refers to the mass of the entire system, is shown as a function of cylindrical radius ϖ/R for several times during the coalescence of Run 1. Here, $R = 10$ km as in Fig. 1.

the source. (For simplicity, we show only one polarization, rh_+ . For all runs presented in this paper, rh_\times is very similar in appearance to rh_+ , with a phase shift of 90° .) The solid line gives the code waveform and the dashed line the point-mass result. The code waveform matches the point-mass case for the first couple of orbits (note that the orbital period is twice the gravitational wave period, $T_{\text{orbit}} = 2T_{\text{GW}}$). As the tidal bulges grow and the stars spiral together faster than they would on point-mass trajectories, the gravitational waves increase in both amplitude and frequency (cf. [33]). Figure 3(b) gives the gravitational wave luminosity L/L_0 , where $L_0 = c^5/G$. The code results (solid lines) initially track the point-mass case (dashed lines), then depart significantly from the point-mass predictions somewhat before the onset of dynamical instability. The amplitudes of the waveforms and luminosity both reach their maximum values during the early stages of the merger at $t \sim 105 - 110t_D$, when the numerical effects discussed above are least important. The amplitudes then decrease as the coalescence proceeds. By $t \sim 180t_D$, the gravitational waves have shut off and the system is essentially axisymmetric.

Table II gives the maximum amplitudes of the gravitational waveforms and luminosities for the runs presented in this paper. For Run 1, we find that the maximum value of the waveform for a source located at distance r from the observer is $(c^2/GM)r|h_{\text{max}}| \sim 2.0(GM/Rc^2)$. For comparison, Rasio and Shapiro ([18]; this is listed as entry RSa in our Table II) found $(c^2/GM)r|h_{\text{max}}| \sim 2.4(GM/Rc^2)$ for a synchronous binary with $\Gamma = 2$. Also, the maximum luminosity is $(L_{\text{max}}/L_0) \sim 0.39(GM/Rc^2)^5$. Rasio and Shapiro found $(L_{\text{max}}/L_0) \sim 0.55(GM/Rc^2)^5$.

The gravitational wave energy spectrum dE/df has proved very useful for analyzing the models in the frequency domain. For point-mass inspiral $dE/df \sim f^{-1/3}$ [28], where the decrease in energy with frequency is due to the fact that the binary spends fewer cycles (and hence emits less energy)

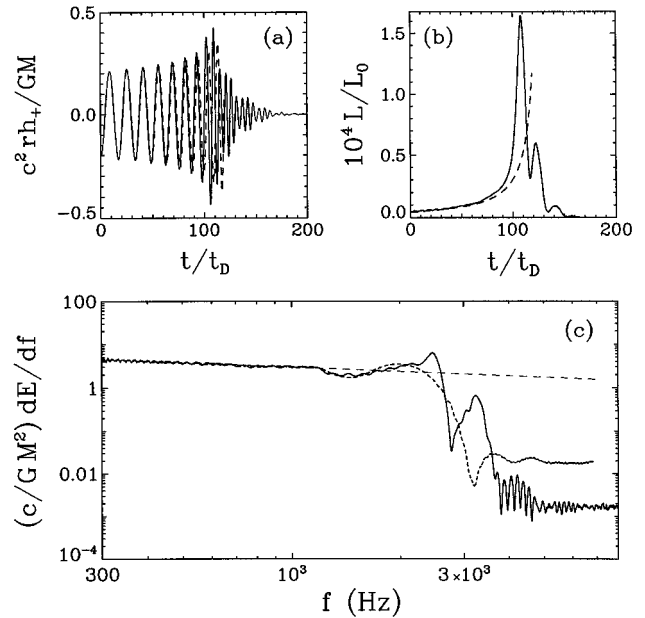


FIG. 3. (a) The gravitational waveform rh_+ for Run 1 is shown for an observer located on the axis at $\theta = \phi = 0$ at distance r from the source. The solid line is the code waveform and the dashed line is the point-mass result. (b) The gravitational-wave luminosity L/L_0 , where $L_0 = c^5/G$. The solid line is the code result, and the dashed line gives the point-mass profile. (c) The gravitational-wave energy spectrum dE/df . The code waveforms have been matched onto point-mass results to produce a long region of point-mass inspiral at low frequencies. The solid line shows the spectrum for the entire run, and the short dashed line shows the spectrum for the waveforms truncated at $t = 120t_D$. The long dashed line is the point-mass spectrum $dE/df \sim f^{-1/3}$.

near a given frequency as it spirals in. Although our runs do start out in the point-mass regime, the stars merge and coalesce within just a few orbits. To achieve a reasonably long region of point-mass inspiral in the frequency domain, we match the code waveforms for all runs in this paper onto point-mass waveforms extending back to much larger binary separations and thus lower frequencies. See paper I for details.

Figure 3(c) shows the energy spectrum dE/df for Run 1. The short dashed line is the spectrum for the waveforms truncated at time $t = 120t_D$; this probes the initial stages of the merger, during which any numerical effects due to Kelvin-Helmholtz mixing should be less important. The solid line shows the spectrum for the full (i.e., untruncated) waveforms. In paper I we defined a number of characteristic frequencies based on features observed in the energy spectrum, and identified these features with various dynamical phases of the coalescence. Starting in the point-mass regime, as f increases, dE/df first drops below the point-mass inspiral value and reaches a local minimum at $f \sim 1500$ Hz. Recall that, for point masses at separation a , the gravitational wave frequency (which is twice the orbital frequency) is given by

$$f_{\text{GW, PM}} = \frac{1}{\pi} \left(\frac{GM}{a^3} \right)^{1/2}. \quad (14)$$

For point-mass inspiral, the frequency at separation

TABLE II. The maximum amplitudes of the gravitational waveform and luminosity are given for each model. The value $(c^2/GM_1)r|h_{\max}| \sim 0.4$ corresponds to an amplitude $h \sim 1.4 \times 10^{-21}$ for a source at distance $r = 20$ Mpc (the approximate distance to the Virgo cluster of galaxies). Scaled versions of these quantities, in terms of the parameter $\alpha \equiv GM_1/R_1c^2$, are also presented. The entries RSa,b, c, and d refer to models of synchronous binaries run by Rasio and Shapiro and are taken from Table I in Ref. [18]. Model RSa has $\Gamma = 2$ and $q = 1$; compare this with our Runs 1, 2, 5, and 6. Model RSb has $\Gamma = 3$ and $q = 1$; this should be compared with our Run 3. Model RSc has $\Gamma = 3$ and $q = 0.85$ and Model RSd has $\Gamma = 3$ and $q = 0.5$; compare these with our Runs 8 and 10, respectively.

Model	$(c^2/GM_1)r h_{\max} $	$(c^2/GM_1)r h_{\max} \alpha^{-1}$	$10^4(L_{\max}/L_0)$	$(L_{\max}/L_0)\alpha^{-5}$
Run 1	0.43	2.0	1.6	0.39
Run 2	0.29	2.1	0.21	0.39
Run 3	0.40	1.9	1.2	0.29
Run 4	0.48	2.3	2.4	0.59
Run 5	0.48	2.3	2.2	0.59
Run 6	0.42	2.0	1.6	0.39
Run 7	0.33	1.6	0.75	0.18
Run 8	0.33	1.6	0.76	0.19
Run 9	0.14	0.67	0.044	0.011
Run 10	0.16	0.76	0.083	0.020
RSa	—	2.4	—	0.55
RSb	—	2.2	—	0.37
RSc	—	1.6	—	0.14
RSd	—	0.8	—	0.018

$a \sim 2.5R$ (where dynamical instability is predicted to set in) is $f_{\text{dyn}} \sim 1500$ Hz. We therefore identify this dip with the onset of dynamical instability.

Beyond f_{dyn} , the spectrum for the truncated waveforms (short dashed line) rises to a local maximum at $f \sim 2000$ Hz, then drops off sharply at higher frequencies. Using Eq. (14), we see that the point-mass gravitational wave frequency at “contact” (i.e., at separation $a = 2R$) is $f_{\text{contact}} \sim 2200$ Hz. We associate the peak with the formation of a rapidly rotating merged system.

The solid line in Fig. 3(c), which shows dE/df for the entire waveforms, contains features characterizing the later stages of the coalescence. We see that the peak shifts to higher frequencies, $f_{\text{peak}} \sim 2500$ Hz, which we attribute to the formation of a transient, rotating barlike structure as the stars coalesce, between $t = 120t_D$ and $t = 150t_D$. Continued shrinking of the merged system as the coalescence proceeds causes the rotation speed of the bar to increase. We note that, if numerical effects due to Kelvin-Helmholtz mixing are shortening the duration of the bar phase of the evolution, our simulations could be substantially underestimating the strength of this feature.

Beyond f_{peak} , the (untruncated) spectrum drops sharply, then rises to a secondary maximum at $f_{\text{sec}} \sim 3200$ Hz. It appears that this feature is due to transient oscillations induced in the merged remnant during coalescence, and therefore this region of the spectrum is undoubtedly influenced by the numerical effects discussed above. We point out that, whether or not the final outcome of actual neutron star coalescence is a black hole, it seems reasonable that a spectrum of quasi-normal mode oscillations will be produced as the remnant “rings down.” Higher resolution simulations that are able to track the detailed mixing of the stars during coalescence, and that fully incorporate general relativity, are needed to calculate this region of the spectrum accurately.

V. BINARIES WITH EQUAL-MASS COMPONENTS

Gravitational radiation from the coalescence of binary neutron stars is expected to contain important information about both the stars themselves and the interaction between them. We have parametrized the binary components as polytropes of masses M_1 and M_2 , radii R_1 and R_2 , spins $\Omega_{s,1}$ and $\Omega_{s,2}$, and equation of state Γ . In this section we present the results of runs with components having equal masses $M_1 = M_2 \equiv M = 1.4M_\odot$ and radii $R_1 = R_2 \equiv R$, and varying R, Γ , and Ω_s . The parameters of these runs are summarized in Table I.

A. Varying the neutron star radius R

Run 2 is the same as Run 1 except that the neutron star radius $R = 15$ km; with $M = 1.4M_\odot$, this gives $GM/Rc^2 = 0.14$. Aspects of this run have already been presented in paper I; we include it here for completeness. In Run 2, the stars start out at initial separation $a_0 = 4R = 60$ km and the gravitational friction terms are turned off at $t = 245t_D$, just before the stars come into contact. As in the standard run rapid coalescence takes place, with mass shed through spiral arms, producing a roughly axisymmetric final remnant.

Figure 4(a) shows the gravitational wave form rh_+ for an observer on the axis at $\theta = \phi = 0$ at distance r from the source. The gravitational wave luminosity L is shown in Fig. 4(b). The maximum amplitudes of the waveforms and luminosity both occur at $t \sim 260t_D$. The maximum value of the waveform (see Table II) for a source located at distance r from the observer is $(c^2/GM)r|h_{\max}| \sim 2.1(GM/Rc^2)$ and the maximum luminosity is $(L_{\max}/L_0) \sim 0.39(GM/Rc^2)^5$; both of these peak amplitudes are essentially the same as those obtained in the standard run.

The gravitational-wave energy spectrum dE/df for Run 2 is shown in Fig. 4(c). For this run, dynamical instability is

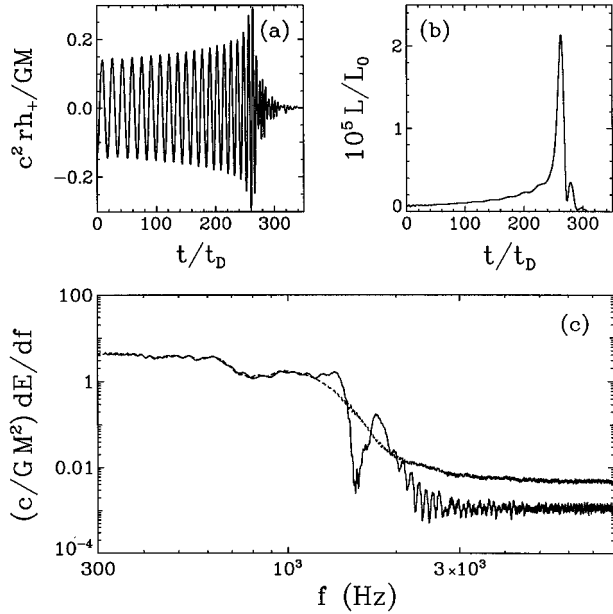


FIG. 4. (a) The gravitational waveform rh_+ for Run 2 is shown for an observer located on the axis at $\theta = \phi = 0$ at distance r from the source. (b) The gravitational-wave luminosity L/L_0 , where $L_0 = c^5/G$. (c) The gravitational-wave energy spectrum dE/df . The solid line shows the spectrum for the entire run, and the dashed line shows the spectrum for the waveforms truncated at $t = 270 t_D$.

expected to occur at separation $a \sim 2.5R$ [33], corresponding to a point-mass inspiral frequency $f_{\text{dyn}} \sim 850$ Hz. As before, this behavior is evident in the data as the spectrum drops below the point-mass value, reaching a minimum at ~ 800 – 900 Hz. The truncated spectrum (dashed line) then rises to a local maximum at $f \sim 980$ Hz before dropping off at higher frequencies. For comparison, the point-mass frequency at separation $a \sim 2R$ is $f_{\text{contact}} \sim 1200$ Hz. The solid line in Fig. 4(c) shows dE/df for the full run; once again, the peak becomes more pronounced and moves to higher frequencies ($f_{\text{peak}} \sim 1350$ Hz) when the late-time waveform is included. Note that the spectrum does not rise above the point-mass result as in Run 1. Nevertheless, it drops sharply just beyond f_{peak} , rising again to a secondary maximum at $f_{\text{sec}} \sim 1800$ Hz. The lack of a strong peak may be due to the weaker tidal forces at the point of dynamical instability, which occurs at a larger physical separation than in Run 1, producing a less-pronounced and shorter-lived bar. As discussed above, numerical effects may well also be weakening this feature.

It is quite instructive to compare the spectra of Runs 1 and 2. Since Eq. (14) gives the frequency of gravitational radiation for point-mass inspiral $\sim a^{-3/2} \sim R^{-3/2}$ at contact, we expect that the characteristic frequencies in the Run 2 spectrum should scale relative to those in Run 1 roughly as $f_2/f_1 \sim 0.54$. Our results for f_{peak} and f_{sec} do show this behavior.

B. Varying the equation of state Γ

Run 3 is the same as Run 1, except that we use a stiffer polytropic equation of state $\Gamma = 3$ ($n = 0.5$). A low-resolution

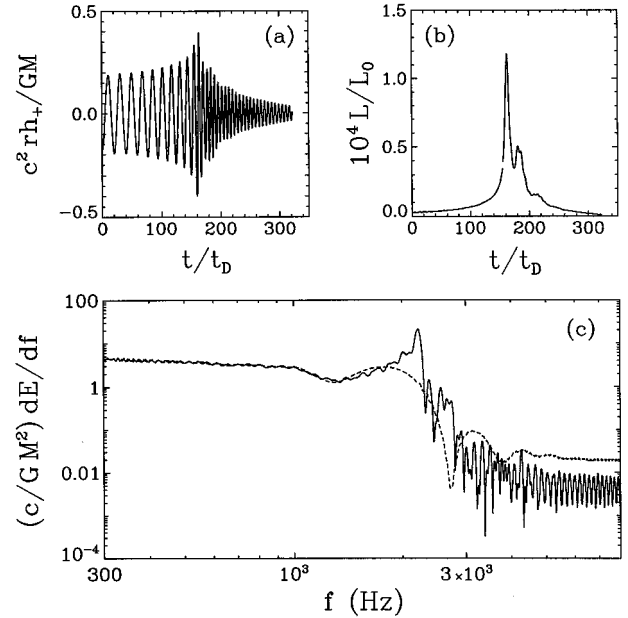


FIG. 5. (a) The gravitational waveform rh_+ for Run 3 is shown for an observer located on the axis at $\theta = \phi = 0$ at distance r from the source. (b) The gravitational-wave luminosity L/L_0 , where $L_0 = c^5/G$. (c) The gravitational-wave energy spectrum dE/df . The solid line shows the spectrum for the entire run, and the dashed line shows the spectrum for the waveforms truncated at $t = 175 t_D$.

version of this run (with $N = 1024$ particles per star) was originally presented in paper I; here we repeat this model with $N = 4096$.

The key difference between the coalescence of equal-mass neutron stars in Runs 1 and 3 is that the core of the final remnant in Run 3 is nonaxisymmetric. This result was also found by Rasio and Shapiro [18] for the case of synchronous binaries with stiff equations of state. As remarked above, uniformly rotating polytropes with $\Gamma > 2.24$ can sustain ellipsoidal shapes, since the mass-shedding limit along a sequence of equilibrium models is reached after the point at which the ellipsoidal sequence bifurcates from the spheroidal sequence. Although the coalesced remnant in Run 3 does have some differential rotation, we expect that this mechanism is operating in this model. In particular, the movement of mass out of the central core region through spiral arms indicates that the system is rotating at the mass-shedding limit. This process is shown in Figs. 1(e)–1(i) for Run 1. In Run 3, the spiral arms are somewhat narrower, as expected for a stiffer equation of state, and the core of the merged remnant is slightly nonaxisymmetric.

The signature of this rotating, nonaxisymmetric core is clearly seen in the gravitational waveform rh_+ , shown in Fig. 5(a). After reaching a maximum value at $t \sim 160 t_D$, the amplitude initially drops rather sharply, and then decays more gradually on a much longer timescale. The luminosity L also reaches its maximum value at $t \sim 160 t_D$, and decreases slowly at late times [see Fig. 5(b)]; we find $(c^2/GM)r|h_{\text{max}}| \sim 1.9(GM/Rc^2)$ and $(L_{\text{max}}/L_0) \sim 0.29(GM/Rc^2)^5$ (see Table II).

For this run, dynamical instability is expected to occur at separation $a \sim 2.76R$ [33], corresponding to a point-mass inspiral frequency $f_{\text{dyn}} \sim 1340$ Hz. Figure 5(c) shows that the

spectrum dE/df for the early stages of the merger (dashed line) drops below the point-mass value and reaches a local minimum near f_{dyn} . It then rises to a local maximum at $f \sim 1800$ Hz, reaching an amplitude above the point-mass value. The spectrum for the entire run (solid line) has a very pronounced peak at $f_{\text{peak}} \sim 2200$ Hz due to contributions from the rotating, nonaxisymmetric core.

As Γ increases the polytrope becomes less centrally condensed, with a larger fraction of its mass in its outer regions. Therefore, tidal effects between the two stars become important at larger separations for $\Gamma=3$ than for $\Gamma=2$ [46]. Dynamical instability is thus predicted to occur at a larger physical separation in Run 3 than in Run 1, and we expect that the spectral features will appear at correspondingly lower frequencies. Using point-mass inspiral we estimate the ratio to be $f_3/f_1 \sim 0.86$, and our results do indeed show this behavior.

Run 4 is the same as Run 1, except that $\Gamma=5/3$ ($n=1.5$) and we used $N=2048$. We note in passing that the equation of state for nuclear matter is generally believed to be stiff, with $\Gamma \geq 2$, and that the case $\Gamma=5/3$ applied to compact objects may be more appropriate for low-mass white dwarfs [47]. Nevertheless, this run allows us to explore the effects of a softer equation of state on binary neutron star coalescence, and we include it here for comparison.

Rasio and Shapiro [47] have shown that, for a synchronous binary composed of equal-mass stars with $\Gamma=5/3$, dynamical instability occurs at separation $a \sim 2.4R$. At this time, the stars in their model were already in contact. In our case, the separation of the centers of mass of the two stars does drop sharply near $a=2.4R$, and the stars are just on the verge of contact at the time. As in Run 1, the stars in Run 4 merge to produce a rotating, axisymmetric final remnant. During this process, spiral arms form and move mass out of the central region into a flattened halo surrounding the central core. The spiral arms in Run 4 appear somewhat wider than in Run 1, as expected, since a softer equation of state is used.

The gravitational waveform rh_+ and the luminosity L are shown in Figs. 6(a) and 6(b), respectively. Both quantities reach their maximum values at $t \sim 115t_D$, with $(c^2/GM)r|h_{\text{max}}| \sim 2.3(GM/Rc^2)$ and $(L_{\text{max}}/L_0) \sim 0.59(GM/Rc^2)^5$.

The spectrum dE/df for Run 4 is shown in Fig. 6(c). Comparison with Fig. 3(c) shows that the spectrum in Run 4 follows the point-mass inspiral result to somewhat higher frequencies, and therefore smaller separations, than in Run 1. This is due to the fact that polytropes with $\Gamma=5/3$ are more centrally condensed than those with $\Gamma=2$, and hence approximate point masses to smaller separations. Using the value $a=2.4R$ as the separation at which dynamical instability takes place, we find $f_{\text{dyn}} \sim 1650$ Hz. The spectrum does dip below the point-mass result to reach a shallow minimum around f_{dyn} , then rises above it to a broad peak at $f \sim 2100$ – 2500 Hz. We estimate f_{peak} for the full spectrum (solid line) to be $f_{\text{peak}} \sim 2300$ Hz. This is followed by a steep drop and a rise to a secondary maximum at $f_{\text{sec}} \sim 4000$ Hz. If we again use the point-mass scaling $f \sim a^{-3/2}$, along with the above value of f_{dyn} , we find $f_4/f_1 \sim 1.05$. Our numerical results give ratios in the range ~ 1.05 – 1.20 .

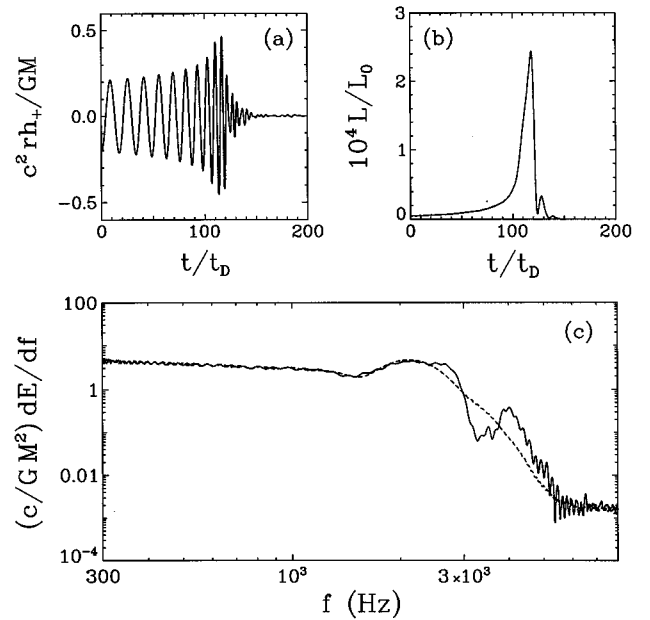


FIG. 6. (a) The gravitational waveform rh_+ for Run 4 is shown for an observer located on the axis at $\theta=\phi=0$ at distance r from the source. (b) The gravitational-wave luminosity L/L_0 , where $L_0=c^5/G$. (c) The gravitational-wave energy spectrum dE/df . The solid line shows the spectrum for the entire run, and the dashed line shows the spectrum for the waveforms truncated at $t=125t_D$.

C. Varying the neutron star spin Ω_s

Thus far, we have studied neutron binary systems in which the components have zero spin at large separations ($a \geq 4R$), as seen from a nonrotating frame. Of course, neutron star binaries are not expected to be synchronously rotating, since the time scale for synchronization is in general much longer than the time scale for orbital decay and inspiral due to gravitational radiation reaction [48]. However, it is very likely on both theoretical and observational grounds that neutron stars are born with nonzero spin, as evidenced by the many short-period pulsars known in the Milky Way galaxy. We have therefore run two models to investigate the effects of spin on the coalescence and the resulting gravitational-wave signals.

The stars used in these models are taken to be uniformly rotating with spin angular velocity Ω_s . They were produced using the method described in [30] (see also [31]), with $N=4055$. (In this method, one does not have complete control over the number of particles accepted into the star; this accounts for the somewhat unusual value of N .) We have chosen $|\Omega_s|=0.175t_D^{-1}$, which is about 30% of the maximum rotation rate that a uniformly rotating neutron star can have before it sheds mass at its equator, $|\Omega_{s,\text{max}}| \leq 0.6t_D^{-1}$ [43,49]. For $M=1.4M_\odot$ and $R=10$ km, this corresponds to a spin period $T_s \sim 2.6$ ms. The stars in our runs have negligible rotational flattening, with the polar radius $\sim 98\%$ of the equatorial radius. Their spins are allowed to be either positive (i.e., parallel to the orbital angular momentum) or negative.

In Run 5, both stars are spinning in the positive sense, with $\Omega_{s,1}=\Omega_{s,2}=0.175t_D^{-1}$ at initial separation $a_0=4R$. The waveform rh_+ reaches its maximum amplitude at $t \sim 105t_D$ as shown in Fig. 7(a). It attains a higher maximum amplitude

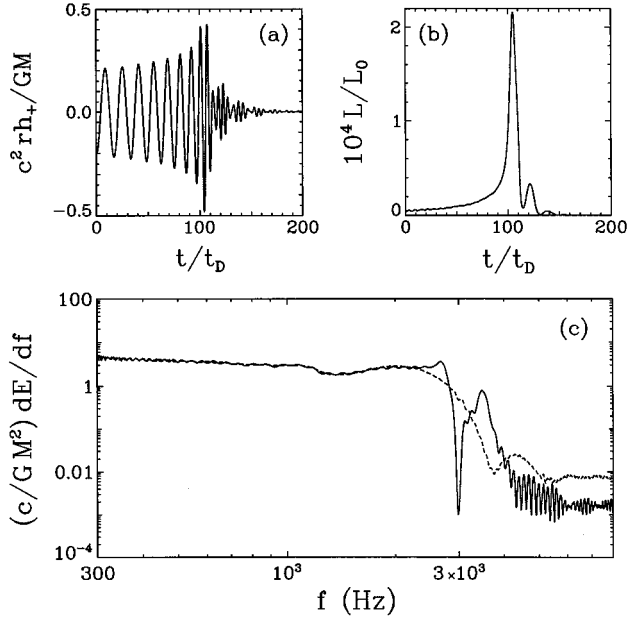


FIG. 7. (a) The gravitational waveform rh_+ for Run 5 is shown for an observer located on the axis at $\theta = \phi = 0$ at distance r from the source. (b) The gravitational-wave luminosity L/L_0 , where $L_0 = c^5/G$. (c) The gravitational-wave energy spectrum dE/df . The solid line shows the spectrum for the entire run, and the dashed line shows the spectrum for the waveforms truncated at $t = 112.5t_D$.

than in Run 1, then drops abruptly to a considerably lower amplitude; cf. Fig. 3(a). The luminosity, which is presented in Fig. 7(b), also reaches a larger maximum value than in Run 1 at $t \sim 105t_D$; see Table II. We find $(c^2/GM)r|h_{\max}| \sim 2.3(GM/Rc^2)$ and $(L_{\max}/L_0) \sim 0.59(GM/Rc^2)^5$. The spectrum dE/df is given in Fig. 7(c). Overall, the spectral features are similar in appearance to those shown in Fig. 3(c) for Run 1. However, both f_{peak} and f_{sec} occur at somewhat higher frequencies in Run 5; see Table III.

TABLE III. Various frequencies of the models relating to the spectra dE/df are given. The frequencies f_{peak} and f_{sec} refer to the spectra calculated from the full waveforms and give the bar rotation speed and the oscillation frequency for the remnant. The truncated spectra peak at somewhat lower frequencies. [The value of f_{peak} given here for Run 2 is somewhat smaller than that used in paper I; the difference is due to some arbitrariness in estimating the location of the ‘‘cliff’’ in Fig. 4(c).]

Model	f_{peak} (Hz)	f_{sec} (Hz)
Run 1	2500	3200
Run 2	1350	1750
Run 3	2200	2600
Run 4	2700	4000
Run 5	2700	3500
Run 6	2500	3200
Run 7	2300	3000
Run 8	2200	2600
Run 9	940	—
Run 10	1000	2300

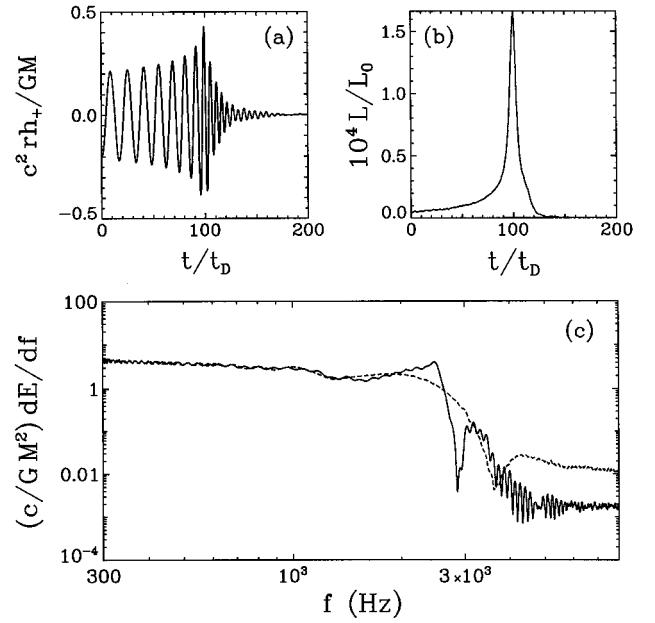


FIG. 8. (a) The gravitational waveform rh_+ for Run 6 is shown for an observer located on the axis at $\theta = \phi = 0$ at distance r from the source. (b) The gravitational-wave luminosity L/L_0 , where $L_0 = c^5/G$. (c) The gravitational-wave energy spectrum dE/df . The solid line shows the spectrum for the entire run, and the dashed line shows the spectrum for the waveforms truncated at $t = 107.5t_D$.

Run 6 is the same as Run 5, except that the stars have spins $\Omega_{s,1} = -\Omega_{s,2} = 0.175t_D^{-1}$. The gravitational waveform [Fig. 8(a)] reaches its maximum amplitude at $t \sim 100t_D$. This maximum value is not as large as that obtained in Run 5, and the subsequent drop in the amplitude of the waveform is more gradual. The luminosity, shown in Fig. 8(b), also reaches a maximum at $t \sim 100t_D$. Here, the maximum luminosity is also somewhat less than in Run 5, although greater than in Run 1, and there is no secondary maximum. In this case we find $(c^2/GM)r|h_{\max}| \sim 2.0(GM/Rc^2)$, $(L_{\max}/L_0) \sim 0.39(GM/Rc^2)^5$. Finally, Fig. 8(c) shows the spectrum dE/df . Comparison with Fig. 3(c) shows that the spectral features for Run 6 are again similar in appearance to those of Run 1 and occur at about the same frequencies. These results are summarized in Table III.

VI. BINARIES WITH UNEQUAL-MASS COMPONENTS

In this section we present the results of simulations with binary components of unequal masses. The primary is taken to have mass $M_1 = 1.4M_\odot$ and radius $R_1 = 10$ km. We then let the secondary have mass $M_2 = qM_1$, where $q = M_2/M_1 < 1$ is the mass ratio. To calculate the radius of the secondary R_2 , we follow Rasio and Shapiro [18] and assume that the system has constant specific entropy. Thus, the initial state of both components is constructed using Eq. (6) with the same polytropic constant $K_1 = K_2$ and the same value of Γ . This gives the mass-radius relation

$$\frac{R_1}{R_2} = \left(\frac{M_1}{M_2} \right)^{(\Gamma-2)/(3\Gamma-4)}. \quad (15)$$

Both components are taken to have zero spin,

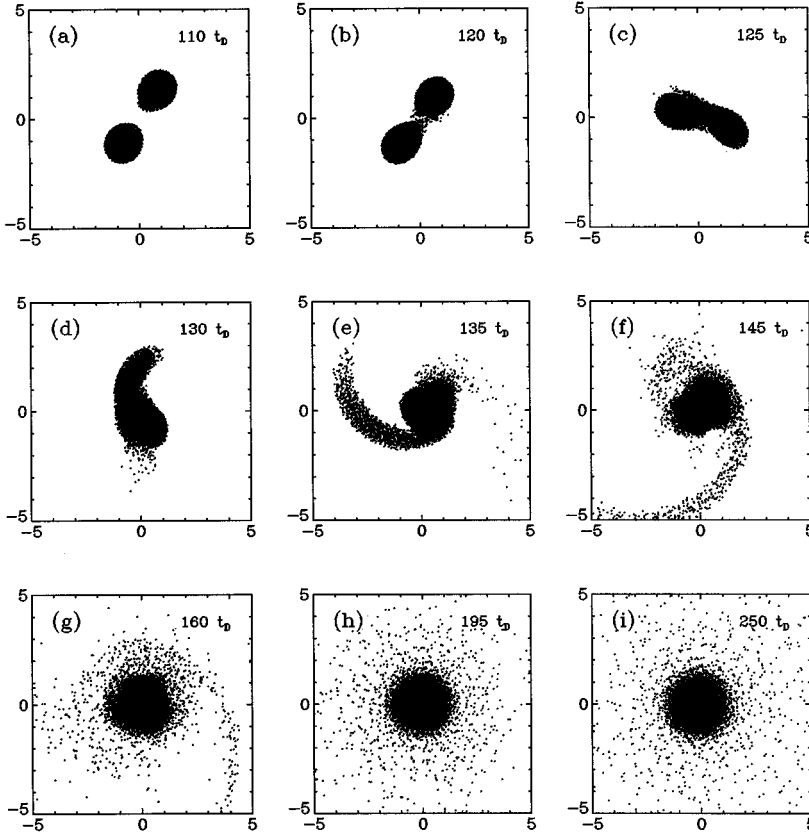


FIG. 9. Particle positions are shown projected onto the x - y plane for Run 7. Here, $M_1=1.4M_\odot$, $M_2=0.85M_1$, $R_1=R_2=10$ km, $\Gamma=2$, and $t_D=0.073$ ms. The initial separation $a_0=4R_1$. The stars are orbiting in the counter-clockwise direction. The vertical axis in each frame is y/R_1 and the horizontal axis is x/R_1 .

$\Omega_{s,1}=\Omega_{s,2}=0$. We use $N=4096$, with all particles in a given star having the same mass. The dynamical time t_D used to describe the evolution of these runs is calculated using the parameters of the primary. Table I summarizes the parameters of these models.

For this paper, we have carried out runs with two different mass ratios, $q=0.85$ and $q=0.5$, using both $\Gamma=2$ and $\Gamma=3$. The value $q=0.85$ is believed to be the most probable mass ratio for the binary pulsar PSR 2303+46 [50]. Although this is the smallest observed value of q for a binary pulsar with a neutron star companion [18], we consider it important at this early stage in our understanding of the gravitational-wave signals from binary coalescence to explore more extreme mass ratios. For this reason we have also considered the case $q=0.5$.

Run 7 is a slightly asymmetric binary with $q=0.85$ and $\Gamma=2$. By Eq. (15), both components have equal radii, $R_2=R_1$. In Fig. 9 all particles are projected onto the x - y plane to show the evolution of this model. Tidal bulges develop as the stars spiral together, and mass transfer begins by $t\sim 120t_D$. As the merger proceeds, a single spiral arm or elongated “tail” is formed from the secondary, seen in Figs. 9(d)–9(g). By the end of the simulation at $t=250t_D$, the secondary has completely merged with the primary. The rotating, axisymmetric remnant has a central core of radius $\sim 1.5R_1$ and is surrounded by a flattened halo consisting of material from the secondary.

The gravitational waveform rh_+ for Run 7 is shown in Fig. 10(a), and the luminosity L is shown in Fig. 10(b). Both quantities reach their maximum amplitudes at $t\sim 125t_D$, during the early stages of the merger. The maximum value of the waveform (see Table II) for a source located at distance

r from the observer is $(c^2/GM)r|h_{\max}|\sim 1.6(GM_1/R_1c^2)$ and the maximum luminosity is $(L_{\max}/L_0)\sim 0.18(GM_1/R_1c^2)^5$. Figure 10(c) shows the gravitational-wave energy spectrum dE/df for this run.

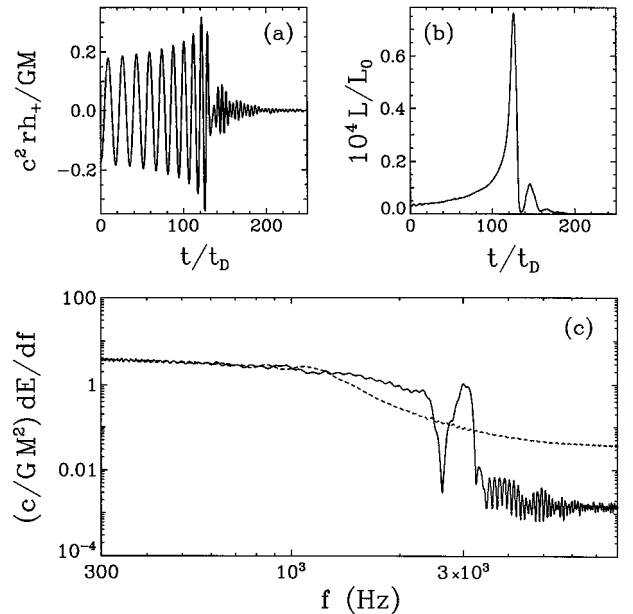


FIG. 10. (a) The gravitational waveform rh_+ for Run 7 is shown for an observer located on the axis at $\theta=\phi=0$ at distance r from the source. (b) The gravitational-wave luminosity L/L_0 , where $L_0=c^5/G$. (c) The gravitational-wave energy spectrum dE/df . The solid line shows the spectrum for the entire run, and the dashed line shows the spectrum for the waveforms truncated at $t=125t_D$.

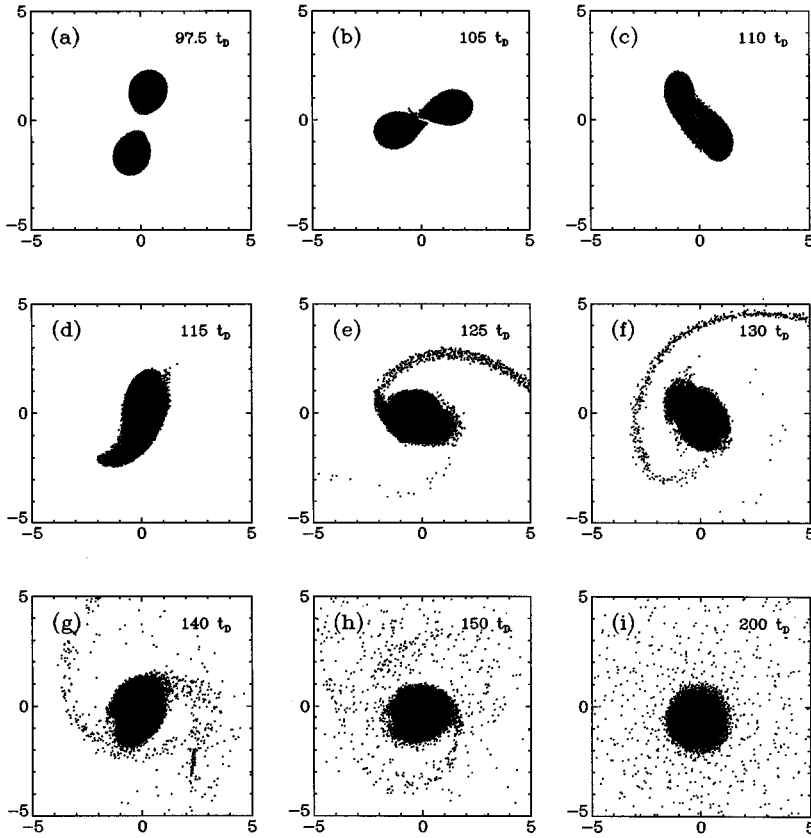


FIG. 11. Particle positions are shown projected onto the x - y plane for Run 8. Here, $M_1=1.4M_\odot$, $M_2=0.85M_1$, $R_1=10$ km, $R_2=9.7$ km, $\Gamma=3$, and $t_D=0.073$ ms. The initial separation $a_0=4R_1$. The stars are orbiting in the counterclockwise direction. The vertical axis in each frame is y/R_1 and the horizontal axis is x/R_1 .

In Run 8 $q=0.85$ and $\Gamma=3$ so that, according to Eq. (15), $R_2=9.7$ km. Figure 11 shows the evolution of this run, which proceeds in a similar way to that in Run 7. In this case, however, the stiffer equation of state leads to a narrower extended tail. The central region also retains an elongated shape for a longer time. By the end of the simulation at $t=200t_D$, the central core is essentially axisymmetric with radius $\sim 1.5R_1$ and a flattened halo composed of mass from the secondary. The remnant is also slightly displaced from the system center of mass. Rasio and Shapiro [18] also notice this behavior in their synchronous merger with $q=0.85$ and $\Gamma=3$, attributing it to the asymmetric, single-arm mass outflow. Interestingly, Run 7 with $\Gamma=2$ also has asymmetric outflow, yet the final remnant suffers a much smaller displacement from the system center of mass.

The gravitational waveform rh_+ for Run 8 is shown in Fig. 12(a), and the luminosity L is shown in Fig. 12(b). Both quantities reach their maximum amplitudes at $t\sim 110t_D$, during the early stages of the merger. More gravitational radiation is produced after the maximum is reached than in Run 7, due to the more strongly nonaxisymmetric central region. The peak value of the waveform (see Table II) for a source located at distance r from the observer is $(c^2/GM)r|h_{\max}|\sim 1.6(GM_1/R_1c^2)$; the maximum luminosity is $(L_{\max}/L_0)\sim 0.19(GM_1/R_1c^2)^5$. Figure 12(c) shows the gravitational-wave energy spectrum dE/df for this run. Comparing the spectrum for the full waveforms with that given in Fig. 10(c) for Run 7, we see that Run 8 with $\Gamma=3$ shows a more pronounced peak at a slightly lower frequency f_{peak} . This behavior is similar to that seen in comparing Runs 1 and 3 and is attributed to the stronger barlike central region; cf. Sec. V B.

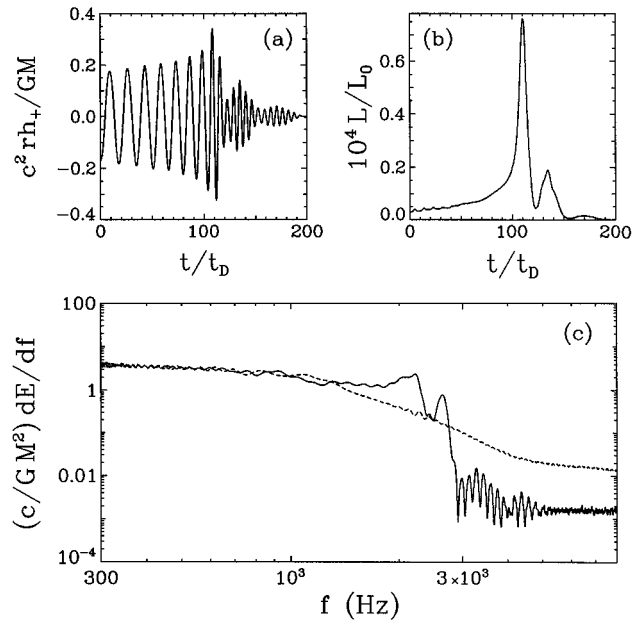


FIG. 12. (a) The gravitational waveform rh_+ for Run 8 is shown for an observer located on the axis at $\theta=\phi=0$ at distance r from the source. (b) The gravitational-wave luminosity L/L_0 , where $L_0=c^5/G$. (c) The gravitational-wave energy spectrum dE/df . The solid line shows the spectrum for the entire run, and the dashed line shows the spectrum for the waveforms truncated at $t=112.5t_D$.

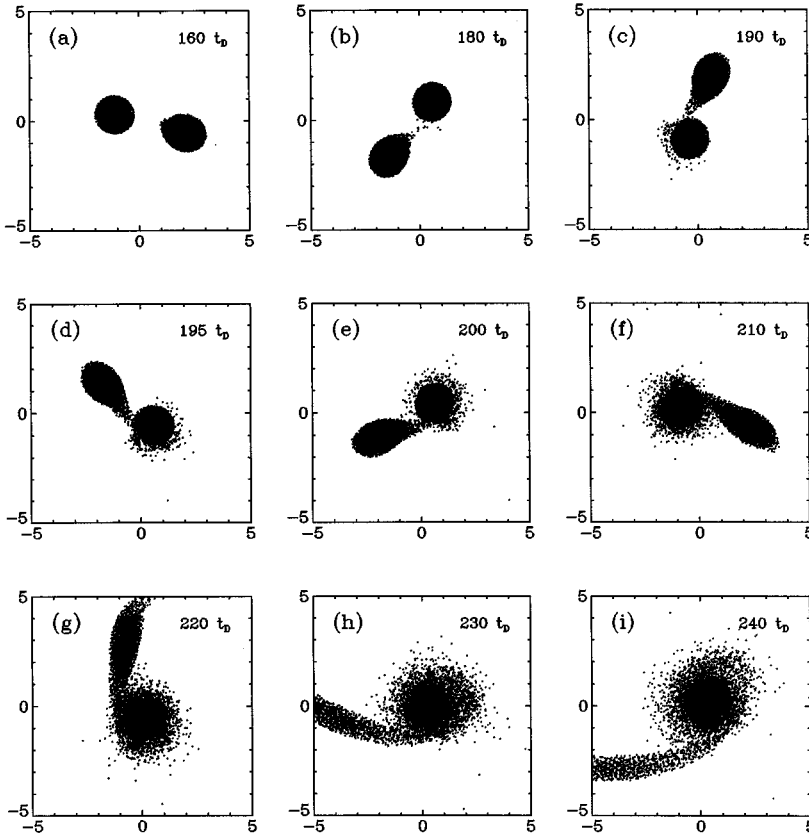


FIG. 13. Particle positions are shown projected onto the $x-y$ plane for Run 9. Here, $M_1 = 1.4M_\odot$, $M_2 = 0.5M_1$, $R_1 = R_2 = 10$ km, $\Gamma = 2$, and $t_D = 0.073$ ms. The initial separation $a_0 = 4R_1$. The stars are orbiting in the counter-clockwise direction. The vertical axis in each frame is y/R_1 and the horizontal axis is x/R_1 .

Run 9 has $q = 0.5$ and $\Gamma = 2$ which implies that the components have equal radii, $R_2 = R_1$. The evolution of this model is shown in Fig. 13, where all particles are projected onto the $x-y$ plane. As the stars spiral together, the secondary develops a tidal bulge and starts to lose mass to the primary. Although this mass transfer completely disrupts the secondary, the primary is not strongly affected. At the end of the run $t = 300t_D$, most of the mass of M_2 is spread in a flattened halo of radius $\sim 5R_1$ around M_1 , with a single spiral arm extending out to very large radii, up to $\sim 40R_1$. The halo and core contain $\sim 96\%$ of the total system mass, and $\sim 70\%$ of the total angular momentum (relative to the center of mass of the system).

Figure 14(a) shows the gravitational waveform rh_+ for this run, and Fig. 14(b) shows the luminosity L . Both the waveform and the luminosity reach their peak values at $t \sim 195t_D$, during the early stages of mass transfer. The gravitational waves shut off less than 1.5 orbits later, indicating that the secondary is quickly disrupted. The maximum value of the waveform (see Table II) for a source located at distance r from the observer is $(c^2/GM)r|h_{\max}| \sim 0.67(GM_1/R_1c^2)$ and the maximum luminosity is $(L_{\max}/L_0) \sim 0.011(GM_1/R_1c^2)^5$. The gravitational-wave energy spectrum dE/df for this run is shown in Fig. 14(c). Since the evolution of the system proceeds rapidly by mass transfer, there is little difference between these two curves, with $f_{\text{peak}} \sim 900$ Hz; there is no discernible high-frequency secondary feature present at late times.

Run 10 uses $q = 0.5$ and $\Gamma = 3$, so $R_2 = 8.7$ km. The evolution of this model is shown in Fig. 15. As before, the tidal bulge on the secondary grows and the resulting mass transfer starts to disrupt it. The primary feels little effect as matter

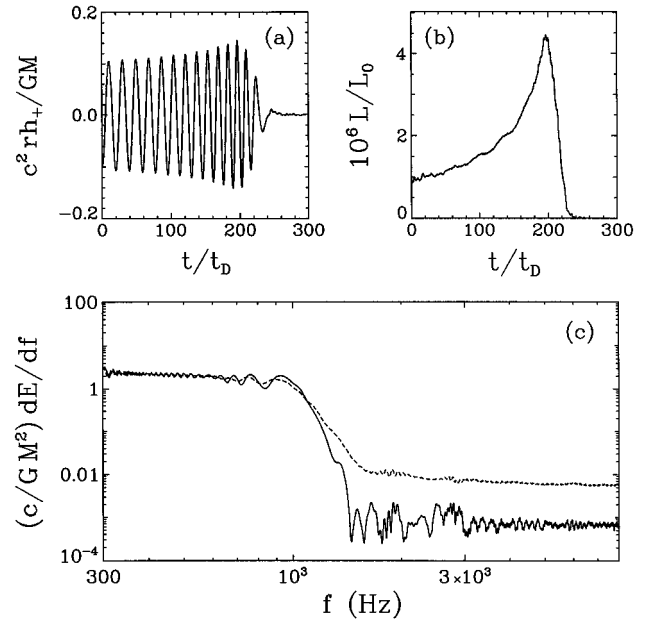


FIG. 14. (a) The gravitational waveform rh_+ for Run 9 is shown for an observer located on the axis at $\theta = \phi = 0$ at distance r from the source. (b) The gravitational-wave luminosity L/L_0 , where $L_0 = c^5/G$. (c) The gravitational-wave energy spectrum dE/df . The solid line shows the spectrum for the entire run, and the dashed line shows the spectrum for the waveforms truncated at $t = 215t_D$.

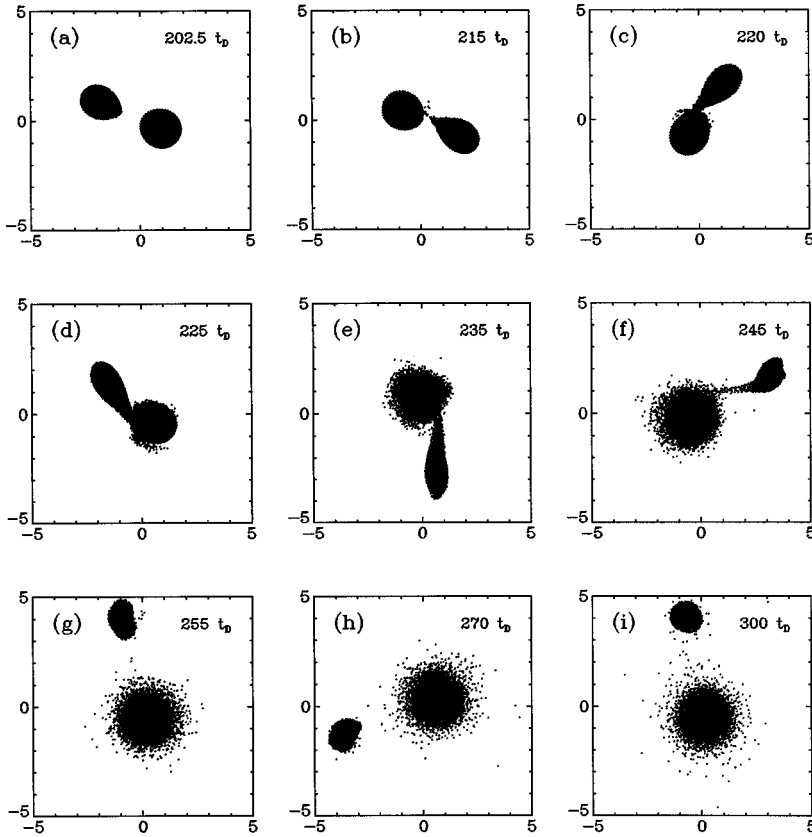


FIG. 15. Particle positions are shown projected onto the x - y plane for Run 10. Here, $M_1 = 1.4M_\odot$, $M_2 = 0.5M_1$, $R_1 = 10$ km, $R_2 = 8.7$ km, $\Gamma = 3$, and $t_D = 0.073$ ms. The initial separation $a_0 = 4.0R_1$. The stars are orbiting in the counterclockwise direction. The vertical axis in each frame is y/R_1 and the horizontal axis is x/R_1 . At the end of the run, frame (i), the secondary has roughly 1/3 of its original mass.

from the secondary spreads around it. However, this period of mass transfer ends $\lesssim 1.5$ orbits after it began when the secondary, now much reduced in size, moves out to a wider orbit. At the end of the simulation ($t = 300t_D$), the primary contains $\sim 86\%$ of the total system mass and has a radius $\sim 1.5R_1$, where R_1 is the initial primary radius. The secondary has a mass $\sim 0.29M_\odot$, about 42% of its original mass, and is in orbit about the primary at center-of-mass separation roughly $\sim 4.5R_1$. Although we ended the simulation at this point, in reality the inspiral will begin again due to gravitational radiation reaction.

The gravitational waveform rh_+ is shown for this run in Fig. 16(a), and the luminosity in Fig. 16(b). Both the waveform and luminosity attain their maximum amplitudes in the early stages of mass transfer at $t \sim 220t_D$. At late times, the waveform shows the signature of the final binary orbit. The maximum value of the waveform (see Table II) for a source located at distance r from the observer is $(c^2/GM)r|h_{\max}| \sim 0.76(GM_1/R_1c^2)$ and the peak luminosity is $(L_{\max}/L_0) \sim 0.02(GM_1/R_1c^2)^5$.

The gravitational-wave spectrum dE/df for Run 10 is given in Fig. 16(c). We find $f_{\text{peak}} \sim 900$ Hz. The spectrum for the full run shows a signal in the region around ~ 600 Hz. Since the point-mass gravitational-wave frequency for the end state of the system at separation $a \sim 4.5R_1$ is ~ 610 Hz, we believe that this feature is due to the final binary orbit. In addition, a high-frequency feature $f_{\text{sec}} \sim 2300$ Hz appears at late times. Since the amplitude of this secondary feature is so much smaller than the main signal around f_{peak} , we suspect that it may be a numerical artifact.

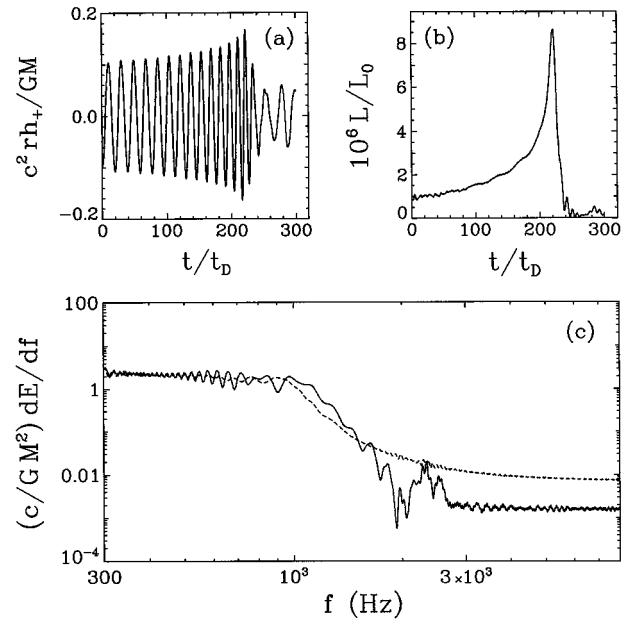


FIG. 16. (a) The gravitational waveform rh_+ for Run 10 is shown for an observer located on the axis at $\theta = \phi = 0$ at distance r from the source. (b) The gravitational-wave luminosity L/L_0 , where $L_0 = c^5/G$. (c) The gravitational-wave energy spectrum dE/df . The solid line shows the spectrum for the entire run, and the dashed line shows the spectrum for the waveforms truncated at $t = 220t_D$.

VII. SUMMARY AND DISCUSSION

We have used SPH to perform 3D simulations of the coalescence of binary neutron stars with the goal of determining the gravitational radiation signals produced and understanding the information that can be extracted from the waveforms, luminosities, and spectra. The stars are initially modeled as spherical polytropes with masses M_1 and M_2 , radii R_1 and R_2 , spins $\Omega_{s,1}$ and $\Omega_{s,2}$, and equation of state Γ , as summarized in Table I. At the start of each run, the stars are placed on (nearly) circular orbits with wide separations so that the binaries are effectively in the point-mass limit. The gravitational field is purely Newtonian, and the gravitational radiation quantities are calculated using the quadrupole approximation. Frictional terms are added to the equations of motion to mimic the effects of gravitational radiation reaction and to cause the stars to spiral together. As the stars get closer, tidal effects grow and eventually dominate. At this point, the frictional terms are turned off and the coalescence proceeds by purely Newtonian hydrodynamics.

Our first set of runs features binaries having components with equal masses $M_1 = M_2 \equiv M = 1.4M_\odot$ and radii $R_1 = R_2 \equiv R$. We varied the radius R , equation of state Γ , and spin Ω_s . In all of these runs, coalescence occurs rapidly once the dynamical stability limit is reached. The merging stars form a rotating barlike structure, and spiral arms are produced as mass is lost from the ends of the bar. Gravitational torques cause angular momentum to be transported outward and lost to the spiral arms. The arms expand supersonically and merge to form a disk around the central object. For the cases that we studied, the rotating core of the final merged remnant is axisymmetric for $\Gamma = 5/3$ and $\Gamma = 2$, and nonaxisymmetric for $\Gamma = 3$.

The gravitational-wave signals for these runs start out following the point-mass results. As the tidal effects grow stronger and the stars begin to spiral in faster than they would on point-mass trajectories, the amplitudes and frequencies of the waveforms and the amplitude of the luminosities increase faster than the point-mass results. These amplitudes reach their maximum values in the early stages of the coalescence, soon after the stars come into contact. Table II shows the scaling relationships for these maximum values for our runs as well as four runs for synchronous binaries by Rasio and Shapiro [18] that are labeled RSa, b, c, and d. For nonspinning stars with $\Gamma = 2$, we find that increasing the value of Γ decreases the strength of these maxima; cf. RSa and RSb. Allowing the stars to have identical spins in the same direction as the orbital angular momentum also increases the maximum values. In particular, our Run 5 gives very similar results to RSa. Interestingly, our Run 6, in which the stars have spins that are equal in magnitude but opposite in direction, produces maximum values that are essentially the same as Run 1 with nonspinning stars.

Examination of the waveforms and luminosities after the maximum values are attained also reveals certain trends. First consider the effects of changing Γ , starting with Run 1 which has $\Gamma = 2$. When we decrease this parameter to $\Gamma = 5/3$ in Run 4, the waves shut off more abruptly than in Run 1, as can be seen by examining Figs. 3(a) and 6(a). We believe that this is due to the tendency for more compressible fluids (i.e., those with smaller values of Γ) to reach the mass-

shedding limit at smaller values of $\beta = T_{\text{rot}}/|W|$. However, when this parameter is increased to $\Gamma = 3$ in Run 3 the waveform amplitude falls off more gradually at late times due to the rotating, slightly nonaxisymmetric core; cf. Figs. 3(a) and 5(a). We attribute this to the ability of polytropes with $\Gamma \gtrsim 2.4$ to sustain ellipsoidal shapes since the mass-shedding limit along a sequence of equilibrium models is reached after the point at which the ellipsoidal sequence bifurcates from the spheroidal sequence. When $\Gamma = 2$ and the stars have parallel spins in the direction of the orbital angular momentum as in Run 5, the amplitude of the waveform drops quite abruptly after the maximum is reached; this is shown in Fig. 7(a). Similar behavior was seen by Rasio and Shapiro [17] and Shibata *et al.* [14]. In Run 6 the spins are antiparallel, and Fig. 8(a) shows that the falloff in the waveform is less abrupt than in the case of parallel spins, but more rapid than in the case of zero spin. In addition, the luminosity drops sharply after reaching its maximum value. All of these runs show three peaks with successively decreasing amplitudes in the luminosity except for Run 6, which has only one peak. The synchronous runs of Rasio and Shapiro [17,18] show a single peak in the luminosity for $\Gamma = 5/3$, 2, and 3, with a secondary peak appearing for $\Gamma = 10$.

The gravitational-wave energy spectrum dE/df is a useful tool for analyzing the models. In the point-mass regime, the spectrum falls off according to $dE/df \sim f^{-1/3}$ [28]. When tidal effects become dominant and the dynamical stability limit is reached, the spectrum drops below the point-mass curve and reaches a local minimum around the corresponding frequency. For the early stages of the merger, the spectrum then rises to a broad local maximum, then falls off rather quickly at higher frequencies. At later times, the peak sharpens and moves to higher frequencies, due to a transient, rotating barlike structure that forms during the coalescence. The spectrum next drops off very sharply, and then rises to a secondary maximum. While we can explain this secondary peak in terms of oscillations in the final remnant, it is unclear how reliable the simulation is at late times. Table III shows that all runs with $R = 10$ km and $\Gamma = 2$ give very similar values for f_{peak} . When $R = 15$ km, these features occur at lower frequencies which scale as expected, roughly as $\sim R^{-3/2}$. Changing the equation of state to $\Gamma = 3$ and using $R = 10$ km produces a somewhat smaller decrease in these frequencies, which we attribute to the occurrence of the dynamical instability at a slightly larger orbital separation.

We performed two simulations with nonequal mass stars having mass ratio $q = 0.85$. In Run 7 with $\Gamma = 2$, the two stars merge to form a remnant that has a central core of radius $\sim 1.5R_1$ surrounded by a flattened halo formed out of matter from the secondary. The behavior of Run 8 with $\Gamma = 3$ is similar, except that the central rotating object remains elongated for a longer period of time. This is reflected in the gravitational-wave spectrum dE/df shown as the solid line in Fig. 12(c), which shows a pronounced peak at $f_{\text{peak}} \sim 2200$ Hz. In contrast, the spectrum for Run 7, which is shown as the solid line in Fig. 10(c), has a much weaker feature at $f_{\text{peak}} \sim 2300$ Hz.

We have also carried out two runs with nonequal mass components having mass ratio $q = 0.5$. In Run 9 with $\Gamma = 2$, the merger proceeds by mass transfer that completely disrupts the secondary. The gravitational waves shut off less

than 1.5 orbits after the maximum amplitude is reached. When $\Gamma=3$, as in Run 10, mass transfer also initially disrupts the secondary. However, less than 1.5 orbits later this process stops as the secondary moves out to a wider orbit. At the end of the run the secondary has $\sim 42\%$ of its original mass and orbits the primary at center-of-mass separation $\sim 4.5R_1$, where R_1 is the initial radius of the primary. Further evolution of this system will proceed on a secular timescale by gravitational radiation reaction. Rasio and Shapiro [18] also report the formation of a detached binary for the case of an initially synchronous system with $\Gamma=3$ and $q=0.5$. Interestingly, their maximum amplitudes for the waveform and luminosity are very similar to ours (although their masses and final orbital separation are not); cf. Runs 10 and RSd in Table II.

It is important to understand the influence of numerical effects on the results of our simulations. In paper I we investigated the use of various artificial viscosity coefficients. We also showed that our results do not depend strongly on N , the number of particles per star, for $N = 1024, 2048,$ and 4096 . However, as discussed in Sec. IV above, we suspect that numerical effects due to Kelvin-Helmholtz instabilities may be influencing the behavior of the shear layer that forms where the two merging stars meet. In particular, the bar phase of the evolution may be artificially shortened and the final remnant may have different properties. These numerical effects should become severe *after* the maximum gravitational radiation amplitudes are reached. Thus, we believe that the scaling of the maximum amplitudes, the shape of the spectrum dE/df for the early stages of the merger, and the approximate location of the frequency f_{peak} are reliable. However, the shape of the gravitational radiation signals after the maximum values are reached, the *strength* of the spectral feature at f_{peak} , and the secondary feature at f_{sec}

may be affected somewhat by numerical processes, and we advise caution when interpreting these results. We remark that the simulations of nonsynchronous binaries carried out by other groups are also expected to suffer from these problems; see Sec. IV. More work is needed to clarify these issues, including simulations with higher resolution.

The gravitational waveforms and spectra resulting from these Newtonian simulations contain much information about the hydrodynamics of the merger. Of course, general relativity is likely to bring in other physical effects that need to be studied in order to understand the data expected from the detectors. For example, Lai and Wiseman [22] have recently shown that the inclusion of certain general relativistic effects along with Newtonian tidal processes causes the neutron stars to begin their final plunge towards merger at larger orbital separations, and hence at lower frequencies, than in the purely Newtonian case. Such information is potentially very important for the detection of the gravitational-wave signals from binary neutron star coalescence by LIGO and other detectors. We intend to incorporate full general relativity in our future work.

ACKNOWLEDGMENTS

We thank N. Andersson, J. Houser, D. Lai, R. Price, F. Rasio, and K. Thorne for interesting and helpful communications, and L. Hernquist for supplying a copy of TREESP. We thank J. Houser for supplying the initial rotating stars used in Runs 5 and 6, and acknowledge the assistance of J. Gao and J. Houser in producing the figures. This work was supported in part by NSF Grants No. PHY-9208914 and No. AST-9308005, and by NASA Grant No. NAGW-2559. The numerical simulations were run at the Pittsburgh Supercomputing Center under Grant No. PHY910018P.

-
- [1] A. Abramovici *et al.*, *Science* **256**, 325 (1992).
 - [2] C. Bradaschia *et al.*, *Nucl. Instrum. Methods Phys. Res. A* **289**, 518 (1990).
 - [3] K. Danzmann *et al.*, in *Relativistic Gravity Research*, Proceedings of the 81WE-Heraeus-Seminar, Bad Hannef, Germany, edited by J. Ehlers and G. Schäfer (Springer-Verlag, Berlin, 1992).
 - [4] R. Narayan, T. Piran, and A. Shemi, *Astrophys. J.* **379**, L17 (1991); E. S. Phinney, *ibid.* **380**, L17 (1991); L. S. Finn and D. Chernoff, *Phys. Rev. D* **47**, 2198 (1993).
 - [5] This subject has been developed by many authors; for a review see C. Will, in *Proceedings of the Eighth Nishinomiya-Yukawa Symposium on Relativistic Cosmology*, edited by M. Sasaki (Universal Academy Press, Japan, 1994).
 - [6] K. Thorne, in *Compact Stars in Binaries*, Proceedings of IAU Symposium 165, edited by J. van Paradijs, E. van den Heuvel, and E. Kuulkers (Kluwer, Dordrecht, 1996).
 - [7] K. Thorne, in *Proceedings of the Snowmass 95 Summer Study on Particle and Nuclear Astrophysics and Cosmology*, edited by E. W. Kolb and R. Peccei (World Scientific, Singapore, 1995); also published in *Particle Physics, Astrophysics & Cosmology*, Proceedings of the SLAC Summer Institute on Particle Physics, edited by Jennifer Chan and Lilian DePorcel (SLAC-Report-484, Stanford Linear Accelerator Center, Stanford, CA, 1996).
 - [8] C. Cutler *et al.*, *Phys. Rev. Lett.* **70**, 2984 (1993).
 - [9] C. Cutler and E. Flanagan, *Phys. Rev. D* **49**, 2658 (1994).
 - [10] B. Meers, *Phys. Rev. D* **38**, 2317 (1988); K. Strain and B. Meers, *Phys. Rev. Lett.* **66**, 1391 (1991); A. Krolak, J. Lobo, and B. Meers, *Phys. Rev. D* **43**, 2470 (1991); **47**, 2184 (1993).
 - [11] W. Johnson and S. Merkowitz, *Phys. Rev. Lett.* **70**, 2367 (1993); G. Harry, T. Stevenson, and H. Paik, *Phys. Rev. D* **54**, 2409 (1996).
 - [12] D. Kennefick, D. Laurence, and K. Thorne (unpublished).
 - [13] L. Lindblom, *Astrophys. J.* **398**, 569 (1992).
 - [14] M. Shibata, T. Nakamura, and K. Oohara, *Prog. Theor. Phys.* **88**, 1079 (1992).
 - [15] See also K. Oohara and T. Nakamura, *Prog. Theor. Phys.* **82**, 535 (1989); **83**, 906 (1990); T. Nakamura and K. Oohara, *ibid.* **82**, 1066 (1989); **86**, 73 (1991).
 - [16] M. Ruffert, H.-Th. Janka, and G. Schäfer, *Astron. Astrophys.* **311**, 532 (1996).
 - [17] F. Rasio and S. Shapiro, *Astrophys. J.* **401**, 226 (1992).
 - [18] F. Rasio and S. Shapiro, *Astrophys. J.* **432**, 242 (1994).

- [19] M. Davies, W. Benz, T. Piran, and F. Thielemann, *Astrophys. J.* **431**, 742 (1994).
- [20] J. Wilson and G. Mathews, *Phys. Rev. Lett.* **75**, 4161 (1995); J. Wilson, G. Mathews, and P. Marronetti, *Phys. Rev. D* **54**, 1317 (1996).
- [21] X. Zhuge, J. Centrella, and S. McMillan, *Phys. Rev. D* **50**, 6247 (1994) (paper I).
- [22] D. Lai and A. Wiseman, *Phys. Rev. D* **54**, 3958 (1996).
- [23] J. Centrella and S. McMillan, *Astrophys. J.* **416**, 719 (1993).
- [24] L. Lucy, *Astron. J.* **82**, 1013 (1977); R. Gingold and J. Monaghan, *Mon. Not. R. Astron. Soc.* **181**, 375 (1977); see J. Monaghan, *Annu. Rev. Astron. Astrophys.* **30**, 543 (1992), for a review.
- [25] L. Hernquist and N. Katz, *Astrophys. J. Suppl. Ser.* **70**, 419 (1989).
- [26] J. Barnes and P. Hut, *Nature (London)* **324**, 446 (1986); L. Hernquist, *Astrophys. J. Suppl. Ser.* **64**, 715 (1987).
- [27] C. Misner, K. Thorne, and J. Wheeler, *Gravitation* (Freeman, New York, 1973).
- [28] K. Thorne, in *300 Years of Gravitation*, edited by S. Hawking and W. Israel (Cambridge University Press, New York, 1987).
- [29] L. S. Finn and C. Evans, *Astrophys. J.* **351**, 588 (1990).
- [30] S. Smith, J. Houser, and J. Centrella, *Astrophys. J.* **458**, 236 (1996).
- [31] J. Houser, Ph.D. thesis, Drexel University, 1996.
- [32] S. Shapiro and S. Teukolsky, *Black Holes, White Dwarfs, and Neutron Stars* (Wiley, New York, 1983).
- [33] D. Lai, F. Rasio, and S. Shapiro, *Astrophys. J.* **420**, 811 (1994).
- [34] D. Lai and S. Shapiro, *Astrophys. J.* **443**, 705 (1995).
- [35] J. S. Turner, *Buoyancy Effects in Fluids* (Cambridge University Press, New York, 1973).
- [36] C.-M. Ho and P. Huerre, *Annu. Rev. Fluid Mech.* **16**, 365 (1984).
- [37] F. Rasio and S. Shapiro, in *Compact Stars in Binaries*, Proceedings of IAU Symposium 165, edited by E. van den Heuvel (in press, 1994).
- [38] F. Rasio (private communication).
- [39] J.-L. Tassoul, *Theory of Rotating Stars* (Princeton University Press, Princeton, NJ, 1973).
- [40] D. Lai, F. Rasio, and S. Shapiro, *Astrophys. J. Suppl. Ser.* **88**, 205 (1993).
- [41] N. Glendenning, F. Weber, and S. Moszkowski, *Phys. Rev. C* **45**, 844 (1992).
- [42] J. Lattimer and F. Swesty, *Nucl. Phys.* **A535**, 331 (1991).
- [43] J. Friedman, J. Ipser, and L. Parker, *Astrophys. J.* **304**, 115 (1986).
- [44] J. Friedman and J. Ipser, *Astrophys. J.* **314**, 594 (1987); F. Weber, N. Glendenning, and M. Weigel, *ibid.* **373**, 579 (1991).
- [45] T. Piran and R. Stark, in *Dynamical Spacetimes and Numerical Relativity*, edited by J. Centrella (Cambridge University Press, New York, 1986).
- [46] D. Lai (private communication).
- [47] F. Rasio and S. Shapiro, *Astrophys. J.* **438**, 887 (1995).
- [48] C. Kochanek, *Astrophys. J.* **398**, 234 (1992); L. Bildsten and C. Cutler, *ibid.* **400**, 175 (1992).
- [49] G. Cook, S. Shapiro, and S. Teukolsky, *Astrophys. J.* **398**, 203 (1992); see also J.-P. Lasota, P. Haensel, and M. A. Abramowicz, *ibid.* **456**, 300 (1996), and references therein.
- [50] S. Thorsett, Z. Arzoumanian, M. McKinnon, and J. Taylor, *Astrophys. J.* **405**, L29 (1993).